Thermal Residual Stress Analysis of Ni–Al2O3, Ni–TiO2, and Ti–SiC Functionally Graded Composite Plates Subjected to Various Thermal Fields

M. Kemal Apalak, Recep Gunes

Thermal Residual Stress Analysis of $Ni–Al_2O_3$, $Ni–TiO_2$, and Ti–SiC Functionally Graded Composite Plates Subjected to Various Thermal Fields

M. KEMAL APALAK* AND RECEP GUNES
Department of Mechanical Engineering
Erciyes University
Kayseri 38039, Turkey

ABSTRACT: This study investigates the thermal elastic residual stresses occurring in $Ni–Al_2O_3$, $Ni–TiO_2$, and Ti–SiC functionally graded plates due to uniform, linear, and parabolic temperature fields through the plate thickness. A 3D eight-noded isoparametric layered (no limit layer number) finite element with three degrees of freedom at each node was implemented to the residual stress problem analogous to the shell elements proposed by Ahmad et al. (Ahmad, S., Irons, B.M. and Zienkiewicz, O.C. (1970). Analysis of Thick and Thin Shell Structures by Curved Finite Elements, *Int. J. of Numerical Methods in Engineering*, **2**: 419–451.) and Yunus and Khonke (Yunus, S.M. and Khonke, P.C. (1989). An Efficient Through-Thickness Integration Scheme in an Unlimited Layer Doubly Curved Isoparametric Composite Shell Element, *Int. J. of Numerical Methods in Engineering*, **28**: 2777–2793.). The longitudinal stresses (σ_{11}, σ_{22}) and transverse shear stresses (σ_{13}, σ_{23}) were dominant. The shear stresses become important especially at the free edges of the plate. As the compositional gradient was increased the normal and shear stresses increased. Whereas the normal stresses become tensile in both ceramic-rich and metal-rich regions; the shear stresses, which are not severe in both the regions, change their directions and become a maximum inside the plate. The thermal and mechanical properties of constituents played an important role on the stress magnitudes rather than on the profiles of the through-thickness variations of normal and shear stresses. Thus, the difference of the coefficients of thermal expansion of the ceramic and metal phases affected the magnitudes of the normal and shear stresses. In addition, the continuous temperature fields through the plate thickness resulted in similar normal and shear stress variations.

KEY WORDS: functionally graded plates, thermal residual stress, layered finite element.

*Author to whom correspondence should be addressed. E-mail: apalakmk@erciyes.edu.tr

0892-7057/05/02 0119–34 $10.00/0 DOI: 10.1177/0892705705043534

INTRODUCTION

LAYERED COMPOSITE MATERIALS have superior thermal and mechanical properties to single-composite material. However, the sharp discontinuity in the material properties along the bimaterial interfaces causes stress concentrations, which may be the main reason of material failure. In order to remove the deficiencies of the layered composite materials, the functionally graded materials (FGM) have been studied extensively since this concept was first introduced by the NKK Corporation in Japan in 1989 when the applications of FGM to thermal-resistant structures of space shuttles were aimed [3].

In the design of FGMs, the main aim is to achieve performance superior to that of single-phase materials by unifying the best properties of the constituent phases. FGM has continuously varying material composition through the material thickness. Therefore, the material composition variation will remove sharp discontinuity between the two material layers; therefore, sudden jumps in the thermal stresses occurring due to different thermal and mechanical properties of the material layers can be minimized.

The thermal and mechanical behaviors of the FGMs are affected by two factors; (i) the thickness-through material properties, such as thermal expansion coefficient and modulus and (ii) the thickness of the FGM layer between the ceramic and the metal layers. Processing or in-service thermal conditions cause significant residual stresses to arise in the FGM as in the joining and composite material problems [4,5]. In order to minimize these thermal residual stresses it is necessary to incorporate the thermal and structural properties of both phases as well as their variation.

Shaw [6] showed thermal residual stresses on both metal and ceramic faces of a compositionally graded plate based on the classical plate theory when a rapid change in volume fraction occurs near the metal face and found that a linear compositional gradient resulted in minimum residual stresses for a uniform temperature distribution.

Reddy [7] presented a theoretical formulation and finite element models based on the third-order shear deformation plate theory for the stress analysis of through-thickness functionally graded plates, which account for the thermomechanical coupling, time dependency, and the von Karman-type geometrical nonlinearity. He showed that the material distribution has an important effect on the deflections and stresses in the functionally graded plates. Reddy and Cheng [8] studied 3D thermomechanical deformations of simply supported functionally graded rectangular plates for different volume fractions of the ceramic and metallic constituents. They found that the assumption of a constant through-thickness deflection usually made by 2D plate theories is invalid for the case of the thermal load.

Cho and Oden [9] studied the effects of the material variation through the thickness and the size of the FGM layer inserted between the metal and the ceramic layers and observed different thermal stress characteristics for different material variations and sizes of FGM. Cho and Ha [10] compared averaging estimation methods with the finite element discretization approach for the thermomechanical properties and responses of dual-phase FGMs, and found that almost all of the averaging estimates produce stress distributions with considerable difference from those by the finite element discritized models. Cho and Ha [11] also optimized the volume fraction for minimizing thermal stresses in FGM by using both penalty-function and golden-section methods.

Grujicic and Zhao [12] investigated the effect of the material concentration profile of a steel–Al_2O_3 graded layer between the pure steel and pure Al_2O_3 regions on redistribution and reduction of thermal residual stresses and material damage. They found that the maximum stresses and damage reductions are achieved for nonlinear material concentration profiles represented by the material concentration exponent $p = 4$. Becker et al. [13] compared analytical and finite element solutions for the thermal stresses in various FGM geometries to the results from their approximate method simplifying to identify desirable types of spatial nonlinearity in expansion coefficient and variations in modulus and allowing the manipulation at the location of compressive stress. Lidong and Wenchao [14] investigated the thermal residual stresses induced on cooling from the sintering temperature of Ti–ZrO_2 FGMs and showed that the graded structure of FGMs can greatly reduce the residual stress compared with nongraded interface of directly jointed materials.

In this study, 3D thermal stress analyses of plates made of Ni–Al_2O_3, Ni–TiO_2, and Ti–SiC FGMs were carried out for the uniform, linear, and parabolic through-thickness temperature distributions. The thermal and mechanical properties of the materials are assumed to vary continuously through the plate thickness between the metal and ceramic phases according to a power-law distribution of the volume fraction of the constituents. In addition, the effect of material composition (metal–ceramic) on the thermal residual stresses was investigated and the optimum material composition through the plate thickness reducing the residual stress was determined.

CONSTITUTIVE RELATIONS

Residual stresses occuring due to thermal and mechanical mismatches of the ceramic and the metal can be reduced and redistributed using a graded interlayer (FGM) between the ceramic and the metal. FGM has continuously varying composition through a dimension of structure from

a ceramic-rich surface to a metal-rich surface. The low thermal conductivity of the ceramic constituent of the material composition provides a high-temperature resistance.

An actual FGM consists of ceramic and metal particles with arbitrary shapes mixed up in random dispersion structures. Thermomechanical properties of an FGM are a function of this shape and orientation of ceramic and metal particles, the dispersion structure as well as the volume fraction. For this purpose, the simple estimation method is the linear rule of mixtures in which a generic material property P at any point ξ in the graded region is determined by the linear combination of volume fractions of ceramic (c) and metal (m) as

$$P(\xi) = V_m(\xi)P_m(\xi) + V_c(\xi)P_c(\xi) \tag{1}$$

providing that

$$V_m + V_c = 1 \tag{2}$$

This method does not consider the effects of particle and dispersion structure, and the interaction between the two constituents. The thermo-mechanical behavior of FGMs is strongly dependent on the accurate estimation of their modulus of elasticity and coefficient of thermal expansion [9,10,15–20].

A functionally graded composite plate composed of a graded layer between homogeneous isotropic ceramic and metal phases is shown in Figure 1. The volume fraction of the metal phase is of the power-law-type

$$V_m(z) = \left(\frac{z + 0.5h}{h}\right)^n \tag{3}$$

where n is the compositional gradient exponent. Figure 2(a) shows the through-thickness variation of the volume fraction of the metal for $n = 0.1$, 0.5, 1.0, 2.0, 5.0, and 10.0 between the ceramic-rich bottom surface and the metal-rich top surface.

Tamura et al. [18] proposed a modified rule-of-mixtures for the modulus of elasticity as

$$E = \left[\left(\frac{q + E_c}{q + E_m}\right)V_m E_m + (1 - V_m)E_c\right]\left[\left(\frac{q + E_c}{q + E_m}\right)V_m + (1 - V_m)\right]^{-1} \tag{4}$$

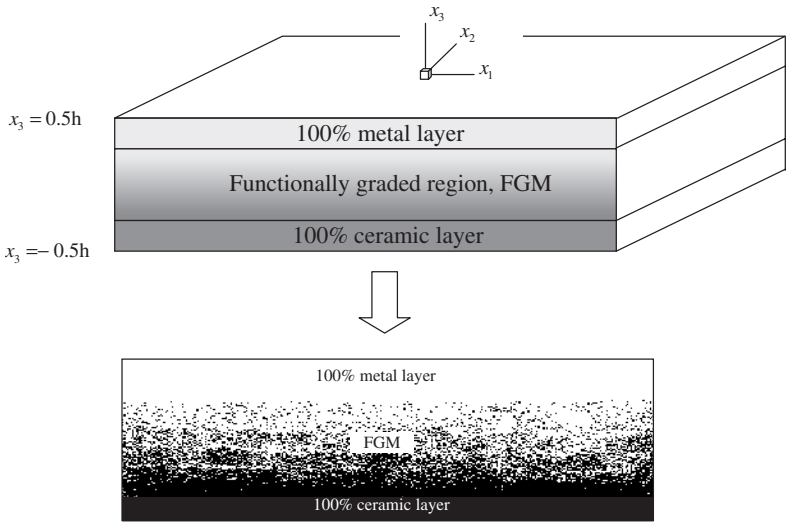

Figure 1. *A functionally graded plate.*

where the stress–strain transfer ratio is

$$q = \frac{\sigma_c - \sigma_m}{\varepsilon_c - \varepsilon_m} \quad \text{where } (0 < q < +\infty) \tag{5}$$

The choice of value q affects the averaged modulus of elasticity based on the modified rule-of-mixtures. For a well-dispersed metal–Al_2O_3 composite, a value q of 500 GPa is recommended [10].

The through-thickness variation of modulus of elasticity of Ni–Al_2O_3 functionally graded plate is shown in Figure 2(b). The thermal and mechanical properties of the constituents of Ni–Al_2O_3 composite material are given in Table 1. For the isotropic particulate composites Wakashima–Tsukamoto [19] expressions require that the overall thermal expansion coefficient for dual-phase materials is related to the averaged bulk modulus using Levin's relation [21]

$$\bar{\alpha} = \alpha_m + \frac{\left(1/\bar{K} - 1/K_m\right)(\alpha_c - \alpha_m)}{1/K_c - 1/K_m} \tag{6}$$

where the overall bulk modulus $\bar{K}$ is

$$\bar{K} = K_m + \frac{aV_cK_m(K_c - K_m)}{V_mK_c + aV_cK_m} \tag{7}$$

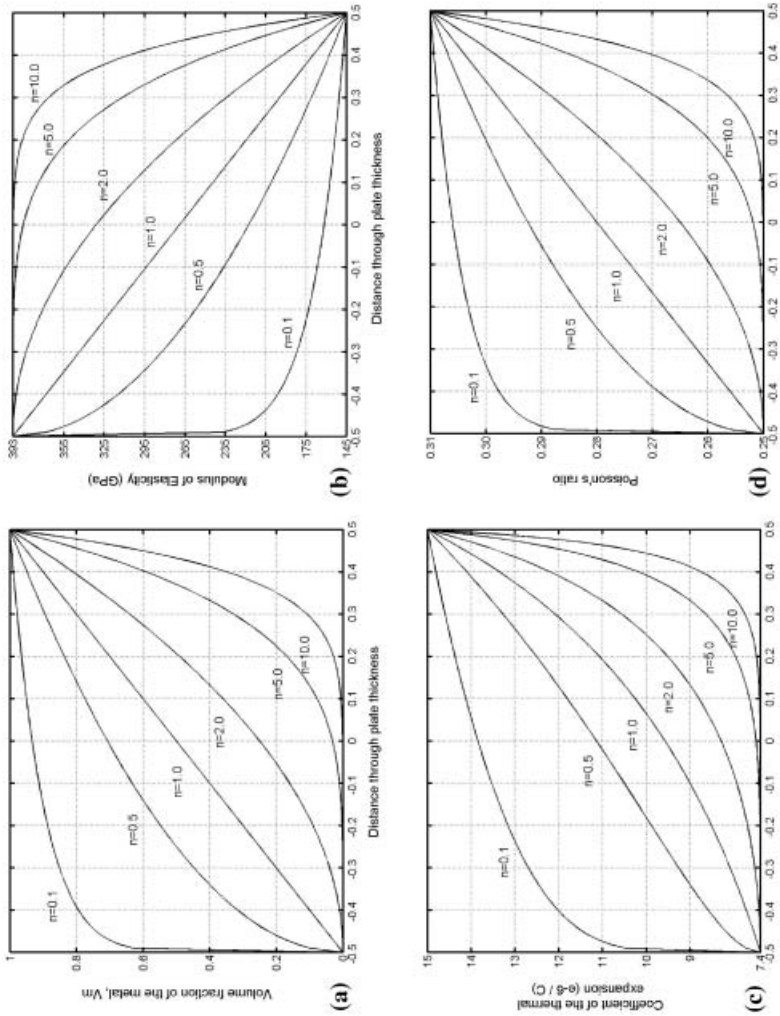

Figure 2. *The through-thickness variations of: (a) volume fraction of metal phase V_m; (b) modulus of elasticity E; (c) the coefficient of thermal expansion α ; and (d) Poisson's ratio ν of a Ni–Al_2O_3 functionally graded plate for different compositional gradient exponents n.*

Table 1. Thermal and mechanical properties of constituents: Ni, Ti, Al_2O_3, TiO_2, and SiC.

	Constituents				
Property	**Ni**	**Ti**	**Al_2O_3**	**TiO_2**	**SiC**
E (GPa)	145	110	393	290	475
α (10^{-6}/°C)	15	10.3	7.4	8.9	4.5
ν	0.31	0.34	0.25	0.27	0.14

and the shear modulus $\bar{\mu}$ is

$$\bar{\mu} = \mu_m + \frac{bV_c\mu_m(\mu_c - \mu_m)}{V_m\mu_c + bV_c\mu_m} \tag{8}$$

and where a and b are

$$a = \frac{K_c(3K_m + 4\mu_m)}{K_m(3K_c + 4\mu_c)}$$

and

$$b = \frac{(1+e)\mu_c}{\mu_m + e\mu_c}$$

together with

$$e = \frac{9K_m + 8\mu_m}{6K_m + 12\mu_m}$$

The overall Poisson's ratio is written as

$$\bar{\nu} = \frac{3\bar{K} - 2\bar{\mu}}{2\left(3\bar{K} + \bar{\mu}\right)} \tag{9}$$

The overall modulus of elasticity alternative to Equation (4) based on the modified rule-of-mixtures can be obtained as

$$\bar{E} = \frac{9\bar{K}\bar{\mu}}{3\bar{K} + \bar{\mu}} \tag{10}$$

The modified rule-of-mixtures for the modulus of elasticity (Equation (4)) will be used.

Figure 2(c) and (d) shows the through-thickness variations of the coefficient of thermal expansion and Poisson's ratio of Ni–Al_2O_3 functionally

graded materials. The through-thickness variations of the mechanical properties of Ni–TiO_2 and Ti–SiC functionally graded plates were not shown here.

FINITE ELEMENT FORMULATION

The potential energy in a linearly elastic body is written as

$$\Pi_p = \int_V \left\{ \frac{1}{2}\{\varepsilon\}^T[D]\{\varepsilon\} - \{\varepsilon\}^T[D]\{\varepsilon_0\} + \{\varepsilon\}^T\{\sigma_0\} \right\} dV - \int_V \{u\}^T\{F\}\, dV - \int_S \{u\}^T\{\phi\}\, dS - \{Q\}^T\{P\} \tag{11}$$

in which $\{u\}$ is the displacement field, $\{\varepsilon\}$ the strain field, $[D]$ the material property matrix, $\{\varepsilon_0\}, \{\sigma_0\}$ the initial strains and stresses, $\{F\}$ the body forces, $\{\phi\}$ the surface tractions, $\{Q\}$ the nodal d.o.f. of the structure, and $\{P\}$ the loads applied to d.o.f. [22].

Displacements within an element are interpolated as from element nodal d.o.f. $\{q\}$

$$\{u\} = [N]\{q\} \tag{12}$$

where $[N]$ is the shape function matrix. Strains are obtained in terms of displacement derivatives as

$$\{\varepsilon\} = [\partial]\{u\} \tag{13a}$$

yields

$$\{\varepsilon\} = [B]\{q\} \tag{13b}$$

where

$$[B] = [\partial][N] \tag{14}$$

Now, Equation (11) yields

$$\Pi_p = \frac{1}{2}\sum_{n=1}^{\text{numel}} \{q\}_n^T[k]_n\{q\}_n - \sum_{n=1}^{\text{numel}} \{q\}_n^T\{r_e\}_n - \{Q\}^T\{P\} \tag{15}$$

where the element stiffness matrix is

$$[k] = \int_{V_e} [B]^T [D][B]\, dV \tag{16}$$

and the element load vector is

$$\{r_e\} = \int_{V_e} [B]^T [D]\{\varepsilon_0\}\, dV - \int_{V_e} [B]^T \{\sigma_0\}\, dV + \int_{V_e} [N]^T \{F\}\, dV + \int_{S_e} [N]^T \{\phi\}\, dS \tag{17}$$

Multilayered 3D Isoparametric Eight-noded Finite Element

An eight-noded, isoparametric 3D finite element has the associated local (ξ_1, ξ_2, ξ_3) and global (x_1, x_2, x_3) coordinate system as shown in Figure 3. The element is composed of N_ℓ layers in its thickness direction ξ_3. The element formulation is based on the 3D elasticity theory and is analogous to

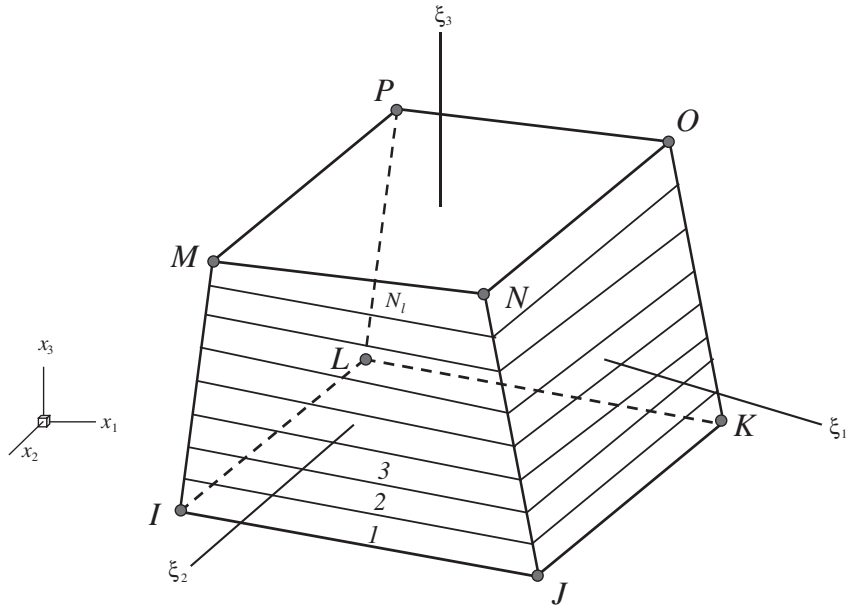

Figure 3. *3D isoparametric layered eight-noded finite element.*

that of the single- and multi-layered curved isotropic shell elements given by Ahmad et al. [1] and Yunus and Khonke [2].

The element geometry is defined by

$$\begin{Bmatrix} x_1 \\ x_2 \\ x_3 \end{Bmatrix} = \sum_{i=1}^{8} N_i \begin{Bmatrix} \xi_1 \\ \xi_2 \\ \xi_3 \end{Bmatrix}_i \tag{18}$$

The displacements u at any point within the element is written in terms of nodal displacements

$$\begin{Bmatrix} u_1 \\ u_2 \\ u_3 \end{Bmatrix} = \sum_{i=1}^{8} N_i \begin{Bmatrix} u_1 \\ u_2 \\ u_3 \end{Bmatrix}_i \tag{19}$$

where N_i is the shape function, and $(u_1)_i,(u_2)_i,(u_3)_i$ are the global nodal displacements. All integration points along the thickness direction ξ_3 are assumed to have the same material orientation.

Strain–Displacement Relations

The strains in terms of the global derivations of displacements are

$$\{\varepsilon\} = [H]\{E\} \tag{20}$$

where

$$\{\varepsilon\} = \begin{Bmatrix} \varepsilon_{11} & \varepsilon_{22} & \varepsilon_{33} & \varepsilon_{12} & \varepsilon_{23} & \varepsilon_{31} \end{Bmatrix}^T$$

$$H = \begin{bmatrix} 1 & 0 & 0 & 0 & 0 & 0 & 0 & 0 & 0 \\ 0 & 0 & 0 & 0 & 1 & 0 & 0 & 0 & 0 \\ 0 & 0 & 0 & 0 & 0 & 0 & 0 & 0 & 1 \\ 0 & 1 & 0 & 1 & 0 & 0 & 0 & 0 & 0 \\ 0 & 0 & 0 & 0 & 0 & 1 & 0 & 1 & 0 \\ 0 & 0 & 1 & 0 & 0 & 0 & 1 & 0 & 0 \end{bmatrix}$$

$$\{E\} = \begin{bmatrix} \begin{bmatrix} E^{(u_1)} \end{bmatrix} & \begin{bmatrix} E^{(u_2)} \end{bmatrix} & \begin{bmatrix} E^{(u_3)} \end{bmatrix} \end{bmatrix}^T$$

$$\begin{bmatrix} E^{(u_1)} \end{bmatrix} = \begin{bmatrix} \dfrac{\partial u_1}{\partial x_1} & \dfrac{\partial u_1}{\partial x_2} & \dfrac{\partial u_1}{\partial x_3} \end{bmatrix}$$

and $[E^{(u_2)}]$ and $[E^{(u_3)}]$ are defined similarly. The global displacement derivatives can be related to the local natural coordinates (ξ_1, ξ_2, ξ_3) as

$$\{E\} = [A]\{e\} \tag{21}$$

where

$$[A] = \text{diag}\left[\, [J]^{-1} \quad [J]^{-1} \quad [J]^{-1} \,\right]$$

$$\{e\} = \left\{ \left[e^{(u_1)}\right] \quad \left[e^{(u_2)}\right] \quad \left[e^{(u_3)}\right] \right\}^T$$

$$\left[e^{(u_1)}\right] = \begin{bmatrix} \dfrac{\partial u_1}{\partial \xi_1} & \dfrac{\partial u_1}{\partial \xi_2} & \dfrac{\partial u_1}{\partial \xi_3} \end{bmatrix}$$

and $[e^{(u_2)}]$ and $[e^{(u_3)}]$ are defined similarly. $[J]$ is the coordinate Jacobian matrix. The local natural coordinate displacement derivatives are expressed in terms of the nodal displacements as

$$\{e\} = \{\eta\}\,\{u_t\} \tag{22}$$

where

$$\{\eta\} = \text{diag}\left[\, [\eta^*] \quad [\eta^*] \quad [\eta^*] \,\right]$$

$$\{\eta^*\} = \begin{bmatrix} \dfrac{\partial N_1}{\partial \xi_1} & \dfrac{\partial N_2}{\partial \xi_1} & . & . & . & \dfrac{\partial N_8}{\partial \xi_1} \\ \dfrac{\partial N_1}{\partial \xi_2} & \dfrac{\partial N_2}{\partial \xi_2} & . & . & . & \dfrac{\partial N_8}{\partial \xi_2} \\ \dfrac{\partial N_1}{\partial \xi_3} & \dfrac{\partial N_2}{\partial \xi_3} & . & . & . & \dfrac{\partial N_8}{\partial \xi_3} \end{bmatrix}$$

$$\{u_t\} = \left[\left[u_t^{(u_1)}\right] \quad \left[u_t^{(u_2)}\right] \quad \left[u_t^{(u_3)}\right] \right]^T$$

$$\left[u_t^{(u_1)}\right] = \left[\, (u_1)_1 \quad (u_1)_2 \quad . \quad . \quad . \quad (u_1)_8 \,\right]$$

$[u_t^{(u_2)}]$ and $[u_t^{(u_3)}]$ are defined similarly.

The matrix Equation (22) is now partitioned and the top part of $\{e^{(u_1)}\}$ can be written as

$$\left\{e^{(u_1)}\right\} = [\eta^*]\left\{u_t^{(u_1)}\right\} \tag{23}$$

Equations (21) and (23) can be combined and expressed as

$$\left\{E^{(u_1)}\right\} = \left[b^{(u_1)}\right]\{\bar{u}\} \tag{24}$$

where

$$\left[b^{(u_1)}\right] = [J]^{-1}[\eta^*]$$

and

$$\{\bar{u}\} = [u]^T$$

$\{E^{(u_2)}\}$ and $\{E^{(u_3)}\}$ are developed similarly and the three are then combined with Equation (20). The strain–displacement relation can be written as

$$\{\varepsilon\} = [B]\{\bar{u}\} \tag{25}$$

where

$$[B] = [H]\begin{bmatrix} \left[b^{(u_1)}\right] \\ \left[b^{(u_2)}\right] \\ \left[b^{(u_3)}\right] \end{bmatrix}$$

$[B]$ contains the inverse of the Jacobian $[J]$.

Stress–Strain Relations

The elasticity matrix $[D]_j$ of layer j is given as

$$[D]_j = \begin{bmatrix} \frac{1}{E_1} & -\frac{\nu_{12}}{E_2} & -\frac{\nu_{13}}{E_3} & 0 & 0 & 0 \\ -\frac{\nu_{12}}{E_2} & \frac{1}{E_2} & -\frac{\nu_{23}}{E_3} & 0 & 0 & 0 \\ -\frac{\nu_{13}}{E_3} & -\frac{\nu_{23}}{E_3} & \frac{1}{E_3} & 0 & 0 & 0 \\ 0 & 0 & 0 & \frac{1}{G_{12}} & 0 & 0 \\ 0 & 0 & 0 & 0 & \frac{1}{G_{23}} & 0 \\ 0 & 0 & 0 & 0 & 0 & \frac{1}{G_{13}} \end{bmatrix}_j \tag{26}$$

In order to provide the continuity of stress between the layers, the elasticity matrix is modified for the layer j as

$$[D^*]_j = \begin{bmatrix} \frac{1}{E_1} & -\frac{\nu_{12}}{E_2} & -\frac{\nu_{13}^*}{E_3^*} & 0 & 0 & 0 \\ -\frac{\nu_{12}}{E_2} & \frac{1}{E_2} & -\frac{\nu_{23}^*}{E_3} & 0 & 0 & 0 \\ -\frac{\nu_{13}^*}{E_3^*} & -\frac{\nu_{23}^*}{E_3^*} & \frac{1}{E_3^*} & 0 & 0 & 0 \\ 0 & 0 & 0 & \frac{1}{G_{12}} & 0 & 0 \\ 0 & 0 & 0 & 0 & \frac{1}{G_{23}} & 0 \\ 0 & 0 & 0 & 0 & 0 & \frac{1}{G_{13}} \end{bmatrix}_j \tag{27}$$

where

$$\nu_{13}^* = E_3^* \left(\frac{\nu_{13}}{E_3}\right)_j, \quad \nu_{23}^* = E_3^* \left(\frac{\nu_{23}}{E_3}\right)_j, \quad \text{and} \quad E_3^* = \frac{t}{\sum_{j=1}^{N_\ell} (t/E_3)_j}$$

t_j is the average thickness of layer j, N_ℓ is the number of layers, and t is the average total thickness of the element.

Stiffness Matrix Formulation

The element stiffness matrix is written in terms of the natural coordinates as

$$[K] = \int_{-1}^{1} \int_{-1}^{1} \int_{-1}^{1} [B]^T [D^*]_j [B] \det [J] \, d\xi_1 \, d\xi_2 \, d\xi_3 \tag{28}$$

where $[D^*]$ is the modified stress–strain matrix at the point of interest within the element.

For a layered element Equation (28) yields [2]

$$[K] = \int_{-1}^{1} \int_{-1}^{1} \sum_{j=1}^{N_\ell} \int_{(\xi_3)_j^{\text{bot}}}^{(\xi_3)_j^{\text{top}}} [B]^T [D^*]_j [B] \det [J] \, d\xi_1 \, d\xi_2 \, d\xi_3 \tag{29}$$

The through-thickness numerical integration is carried out modifying the variable ξ_3 to $(\xi_3)_j$ in the jth layer such that ξ_3 varies from -1 to 1 in that layer [23,24].

$$\xi_3 = -1 + \frac{1}{t}\left[2\sum_{k=1}^{j} h_k - h_j(1 - \xi_{3j})\right] \tag{30}$$

and

$$d\xi_3 = \frac{h_j}{t}\, d\xi_j \tag{31}$$

Substituting Equations (30) and (31) in Equation (29) yields

$$[K] = \int_{-1}^{1}\int_{-1}^{1}\sum_{j=1}^{N_\ell}\int_{-1}^{1} [B]^T [D^*]_j [B] \det [J] \left(\frac{h_j}{t}\right) d\xi_1\, d\xi_2\, d\xi_3 \tag{32}$$

a $2 \times 2 \times 2$ Gauss integration scheme is needed for each layer in order to evaluate the contribution of that layer to the stiffness of the element.

Thermal Load Vector

In order to derive the thermal load vector a biquadratic distribution of temperatures is assumed on the top (MNOP) and bottom (IJKL) faces and a linear variation through its thickness (see Figure 3). The thermal strain at a point (ξ_1, ξ_2) in the layer j is then given as

$$\left\{\varepsilon^{\text{th}}\right\}_j = \{\alpha\}_j [T_1 + \xi_3 T_2 - T_{\text{ref}}] \tag{33}$$

where

$$\{\alpha\}_j = \begin{bmatrix} \alpha_1 & \alpha_2 & \alpha_3 & 0 & 0 & 0 \end{bmatrix}_j^T$$

$(\alpha_1)_j$, $(\alpha_2)_j$, and $(\alpha_3)_j$ are coefficients of thermal expansion in the x_1-, x_2-, and x_3-directions, respectively. For the layer j

$$T_1 = \frac{T^t + T^b}{2} \quad \text{and} \quad T_2 = \frac{T^t - T^b}{2} \tag{34}$$

where T^t and T^b are the temperatures at the top and bottom faces of the element at the point (ξ_1, ξ_2). The thermal strain vector in Equation (33) is

written as

$$\left\{\varepsilon^{\text{th}}\right\}_j = \xi_3\left\{\varepsilon_1^{\text{th}}\right\}_j + \xi_3\left\{\varepsilon_2^{\text{th}}\right\}_j \tag{35}$$

where

$$\left\{\varepsilon_1^{\text{th}}\right\}_j = \{\alpha\}_j(T_1 - T_{\text{ref}})$$

$$\left\{\varepsilon_2^{\text{th}}\right\}_j = \{\alpha\}_j T_2$$

The consistent thermal load vector is given as

$$\left\{F^{\text{th}}\right\} = \int_V [B]^T[D^*]\{\varepsilon_{\text{th}}\}\, dV \tag{36}$$

and for the layered element as

$$\left\{F^{\text{th}}\right\} = \sum_{j=1}^{N_L} \int_V [B]^T[T_m]_j^T[D^*]_j\left\{\varepsilon_j^{\text{th}}\right\} d(V_j) \tag{37}$$

where V_j is the volume of the layer j and $[T_m]$ is the transformation matrix from the global (x_1, x_2, x_3) to the local (ξ_1, ξ_2, ξ_3) coordinate systems [2].

NUMERICAL RESULTS

In this study, the thermal residual stresses in the functionally graded plates with various constituents induced by cooling from a high temperature field were investigated using the present 3D layered finite element. For this purpose, a plate with a small unit thickness in comparison with other dimensions is considered (Figure 1). The bottom and top surfaces of the plate are assumed to be ceramic and metal, respectively. A functionally graded region was introduced between the ceramic and the metal layers in order to reduce the thermal stress distribution through the plate thickness. The residual stresses during cooling occur due to the thermal and mechanical mismatches of the constituents of the layer. The composition of constituents and the thermal field play important roles on the thermal residual stresses in the plate. The residual stresses in functionally graded plates composed of constituents Ni–Al_2O_3, Ni–TiO_2, and Ti–SiC were investigated during the cooling periods for the through-thickness (i) uniform, (ii) linear, and (iii) parabolic temperature distributions. The layers were assumed to be bonded perfectly and elastic and the plate was strain-free initially.

In order to show the performance of the layered finite element, an one-fourth model of the plate was used due to its symmetry, and the plate geometry was meshed. Since the edges of the plate were divided into 10 segments and 20 segments were used through the plate thickness, the plate model had 2000 layered finite elements. The thermal residual stress analysis of the plate composed of a material system Ni–Al_2O_3 subjected to a uniform temperature field was repeated by increasing the number of layers in each layered finite element, i.e., 20–2500 as shown in Table 2. In addition, the stress analysis was also carried out for the Ni–Al_2O_3 functionally graded plate which was modeled by using a 3D solid finite element with three d.o.f. at each node. However, in order to obtain the same layer thickness, the plate was divided into 20–2500 finite elements. Consequently, the number of d.o.f. and nodes were increased considerably (Table 2). The stress analyses were carried out in a PC having 1.6 MHz CPU speed and 512 Mb RAM, and the CPU time of the solutions are also shown in Table 2. Due to hardware limitations a solution was not achieved for the plate models including more finite elements than 80 through the plate thickness whereas the number of the finite elements, nodes, and d.o.f. remain constant in the plate models composed of the layered finite elements. In addition, a considerable increase in the CPU time for the solutions was not observed for the layered finite elements. It is evident that a classical 3D solid finite element may be not suitable for this type of problem (Table 2).

Based on these tests, in this study a one-fourth model of the plate was used due to its symmetry, and the plate geometry was meshed by using the

Table 2. Comparison of the performance tests of the 3D solid finite element and the 3D layered finite element.

Number of layer	Element type	Number of node	Number of element	d.o.f	CPU time
20	Layered	2541	2000	7623	5.875
	Solid	2541	2000	7623	4.078
40	Layered	2541	2000	7623	5.875
	Solid	18,081	16,000	54,243	64.859
80	Layered	2541	2000	7623	6.344
	Solid	136,161	128,000	408,483	3094.266
100	Layered	2541	2000	7623	6.453
200	Layered	2541	2000	7623	7.469
400	Layered	2541	2000	7623	9.093
1000	Layered	2541	2000	7623	14.203
2000	Layered	2541	2000	7623	22.244
2500	Layered	2541	2000	7623	26.328

present layered finite element, i.e., $10 \times 10 \times 20$ uniform elements. Each finite element included 125 layers; therefore, the through-thickness compositional variation of the plate thickness was modeled with 2500 layers. The layer thickness becomes 0.4 μm. For all thermal conditions the reference temperature was 25°C, the top and bottom surface temperatures were 800 and 1000°C, respectively.

Uniform Temperature Field

In order to determine the thermal stress state of a functionally graded plate with a specified thickness-through compositional variation, first a Ni–Al_2O_3 system was considered. For a uniform temperature field through the plate thickness specified as

$$\Delta T = -975^{\circ}\mathrm{C} \tag{38}$$

the stress analysis of the Ni–Al_2O_3 functionally graded plate was carried out for the through-thickness composition variations corresponding to the compositional gradient exponents $n = 0.1$, 1.0, and 10.0. The normal stress σ_{11}, σ_{22}, σ_{33} and shear stress σ_{12}, σ_{23}, σ_{13} distributions through the plate are shown in Figures 4–6 for the compositional gradient exponents $n = 0.1$, 1.0, and 10.0, respectively.

In the case of $n = 0.1$, the ceramic-rich face experiences considerable compressive normal stress σ_{11} and σ_{22} distributions (Figure 4(a) and (b)). Since the metal constituent Ni is dominant in the through-thickness compositional variations, the plate is subjected to a low stress distribution, except the ceramic-rich surface and its vicinity. The normal stress σ_{33} is less severe in comparison with the normal stresses σ_{11} and σ_{22} (Figure 4(c)). The free plate corner experiences low shear stress σ_{12} concentrations (Figure 4(d)), and the shear stresses σ_{23} and σ_{13} uniformly varying through the plate thickness become considerable (Figure 4(e) and (f)).

In the case of $n = 1.0$, the normal stress σ_{11}, σ_{22}, σ_{33} and shear stress σ_{12}, σ_{23}, σ_{13} distributions through the Ni–Al_2O_3 functionally graded plate under uniform temperature field are shown in Figure 5. Whereas the ceramic-rich surface is in compression the metal-rich surface is in tension. However, the normal stress distributions through the plate thickness (Figure 5(a)–(c)) are low and continuous in comparison with those of $n = 0.1$ (Figure 4(a)–(c)). Thus, a linear through-thickness compositional variation results in the tensile normal stresses in the ceramic-rich surface contrary to the compressive normal stresses in the case of $n = 0.1$ and the tensile normal stresses in the metal-rich surface are still higher. The

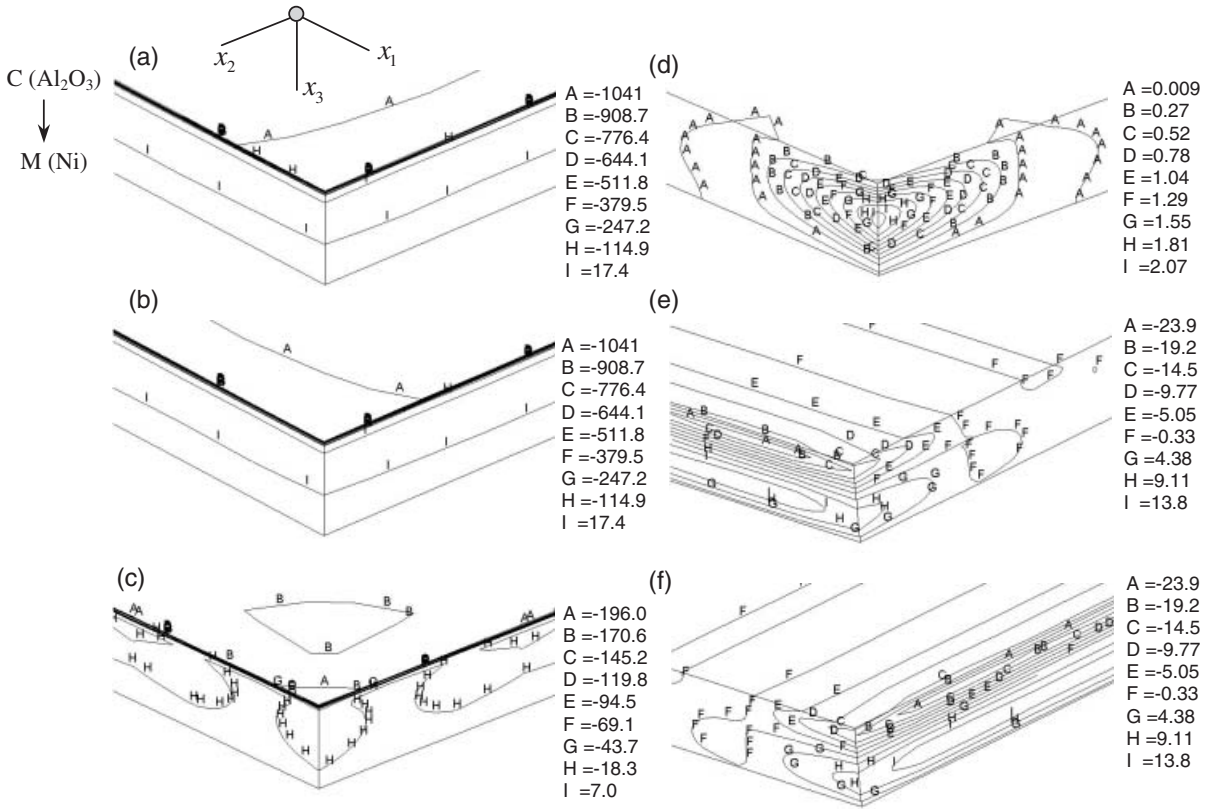

Figure 4. *The normal stress: (a) σ_{11}; (b) σ_{22}; (c) σ_{33} and shear stress: (d) σ_{12}; (e) σ_{23}; (f) σ_{13} distributions in a Ni–Al_2O_3 functionally graded plate subjected to a uniform temperature field ($n = 0.1$) (all stresses in MPa).*

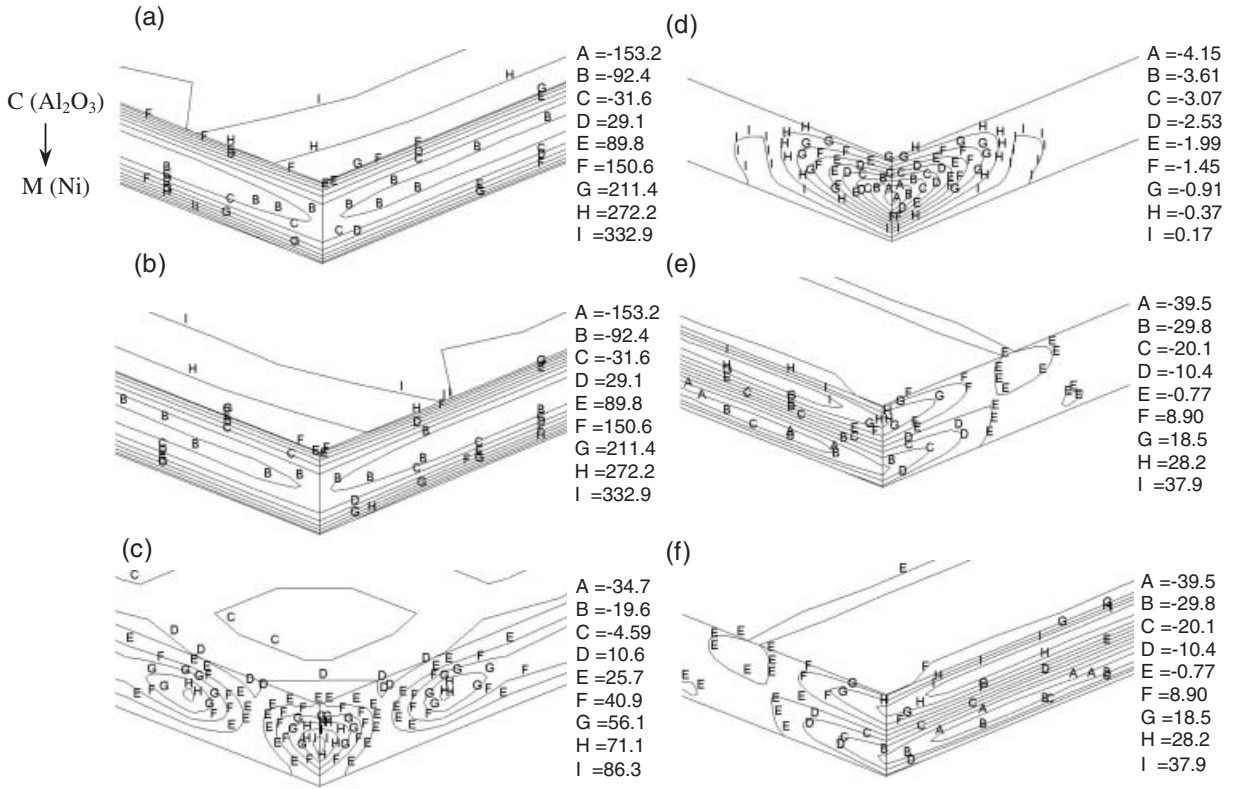

Figure 5. *The normal stress: (a) σ_{11}; (b) σ_{22}; (c) σ_{33} and shear stress: (d) σ_{12}; (e) σ_{23}; (f) σ_{13} distributions in a Ni–Al_2O_3 functionally graded plate subjected to a uniform temperature field ($n = 1.0$) (all stresses in MPa).*

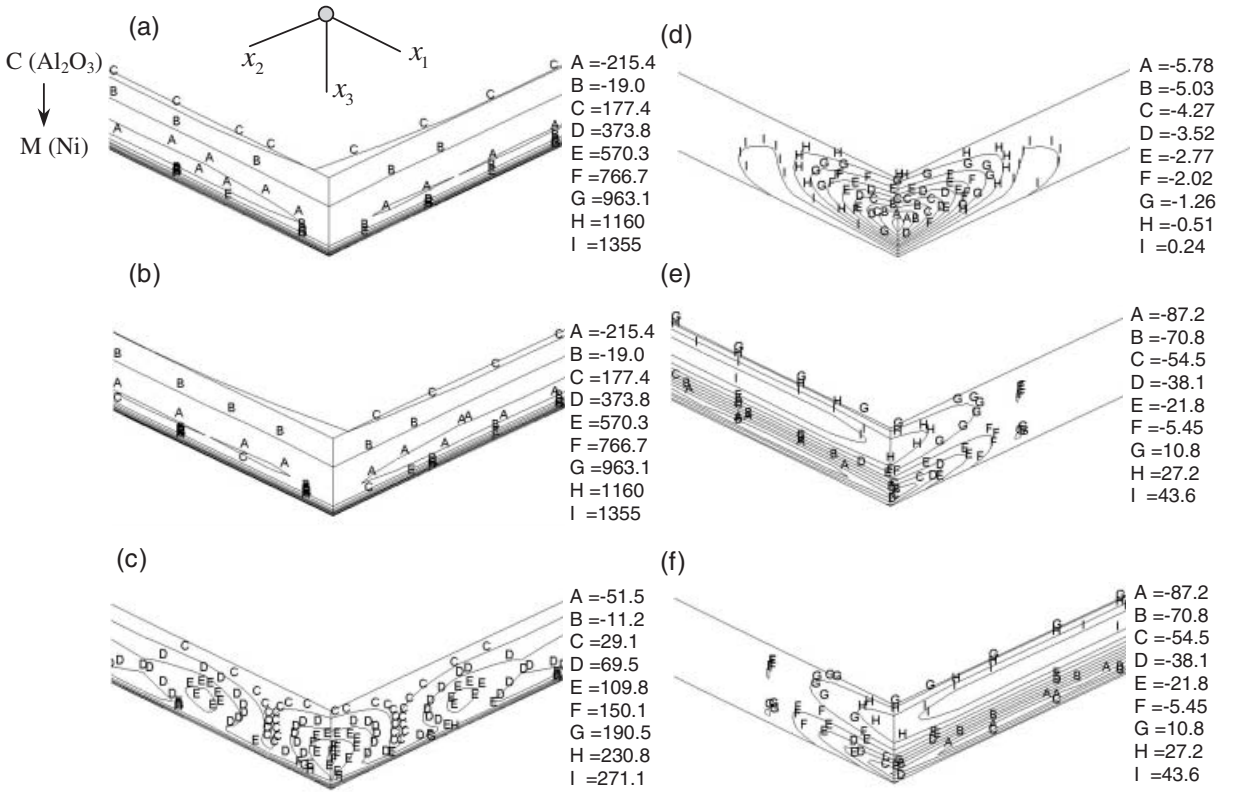

Figure 6. *The normal stress: (a) σ_{11}; (b) σ_{22}; (c) σ_{33} and shear stress: (d) σ_{12}; (e) σ_{23}; (f) σ_{13} distributions in a Ni–Al_2O_3 functionally graded plate subjected to a uniform temperature field ($n = 10.0$). (All stresses in MPa).*

middle region across the plate thickness is also subjected to compressive stresses.

However, the through-thickness distributions of the shear stresses σ_{12}, σ_{23}, and σ_{13} are not affected by the compositional gradient exponent (n) considerably. Thus, balanced shear stress σ_{23} and σ_{13} distributions through the plate thickness are observed. In addition, an evident increase in all peak shear stress components appears to be about 125%.

In the case of $n = 10.0$, the tensile normal σ_{11} and σ_{22} stresses concentrate on the metal-rich surface and increase considerably, whereas the remaining region through the plate thickness experiences lower tensile stresses. The normal σ_{11} and σ_{22} stresses are compressive over most of the middle region of the plate thickness, and the tensile normal σ_{33} stress reaches a considerable level (Figure 6(a)–(c)).

Similarly, the shearing stresses σ_{23} and σ_{13} become more uniform through the plate thickness and get maximum values in the metal-rich surface. In addition, they act in the reverse direction along the distance from the metal-rich surface to the ceramic-rich surface. The shear stress σ_{12} concentrates around the plate free corner. However, it is not so severe as the shear stress σ_{23} and σ_{13} components (Figure 6(d)–(f)).

As seen, the through-thickness variations and levels of the normal and shear stresses are affected considerably by the compositional gradient exponent "n". Therefore, this implies that an optimum composition variation through the plate thickness may be possible so as to obtain a reasonable residual stress distribution.

The Effect of the Compositional Gradient Exponent "*n*"

In order to determine the effect of the compositional gradient exponent "n" on the through-thickness variations of normal and shear stresses, thermal stress analyses of Ni–Al_2O_3, Ni–TiO_2, and Ti–SiC functionally graded plates subjected to a uniform temperature field were carried out for $n = 0.1$, 0.5, 1.0, 2.0, 5.0, and 10.0. Since the longitudinal stresses σ_{11} and σ_{22} exhibit similar distributions (Figures 4–6), the through-thickness variations of only longitudinal stress σ_{11} are plotted in Figures 7, 9, and 11 for the Ni–Al_2O_3, Ni–TiO_2, and Ti–SiC functionally grade plates, respectively.

Ni–Al_2O_3 SYSTEM

In the case of a Ni–Al_2O_3 functionally graded plate with $n = 0.1$ (see Figure 7(a)) the longitudinal stress σ_{11} is compressive on both the metal-rich and the ceramic-rich surfaces and a large region in the middle of the plate thickness is in tension. $n = 0.5$ results in lower compressive stresses on the ceramic surface and tensile stresses on the metal surface. In addition, two regions in

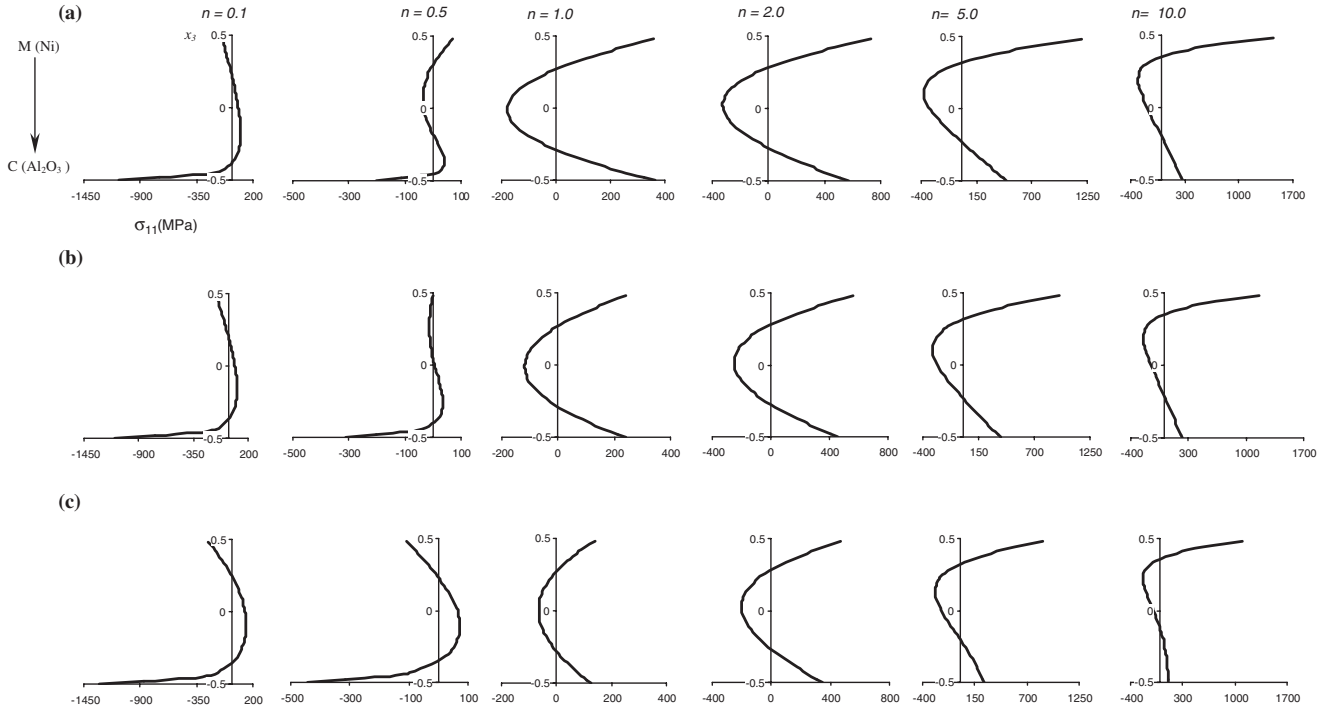

Figure 7. *The effect of the compositional gradient exponent n on the through-thickness variation of the longitudinal stress σ_{11} in Ni–Al_2O_3 functionally graded plates subjected to: (a) uniform; (b) linear; and (c) parabolic temperature fields (stresses in MPa).*

compression and tension between the ceramic and the metal layers appeared. However, the normal stresses become maximal on the ceramic surface. For $n = 1.0$ and 2.0, a uniform normal stress σ_{11} distribution through the plate thickness is observed, and both the ceramic-rich and the metal-rich surfaces undergo nearly same tensile stress levels whereas the middle plate region is in compression. However, for the functionally graded plates with $n = 5.0$ and 10.0, the normal stress σ_{11} levels increase on the metal-rich surface whereas it decreases slightly on the ceramic side. It is important that a smaller compositional gradient exponent than 1.0 results in considerable compressive normal stress σ_{11} in the ceramic phase region and negligible tensile normal stress σ_{11} in the metal phase region. For $n > 1.0$, longitudinal stress σ_{11} becomes tensile on both the ceramic and the metal layers.

For a uniform temperature distribution through the plate thickness the transverse shear stress components σ_{23} and σ_{13} are dominant in a Ni–Al_2O_3 functionally graded plate (see Figures 4–6) for $n = 0.1$, 0.5, and 10.0, respectively. Accordingly, the effect of the compositional gradient exponent "n" on the through-thickness variation of the transverse shear stress σ_{13} in a Ni–Al_2O_3 functionally graded plate is only shown in Figure 8(a). The shear stress σ_{13} levels are low 24–27 times in comparison with the longitudinal stress σ_{11} (Figure 7(a)). $n = 0.1$ results in a parabolic variation through the plate thickness; thus, there is one plane along which the shear stress σ_{13} becomes zero and two regions having shear stress variations in opposite directions. As the compositional gradient exponent n is increased it is observed that the shear stress σ_{13} increases in magnitude but acts on the opposite direction. Consequently, the transverse shearing stress σ_{13} distribution becomes minimum for $n = 0.5$ and maximum for $n = 10.0$.

However, the peak shearing stress σ_{13} does appear neither in the ceramic phase region nor in the metal phase region, it occurs at locations near one-quarter of the plate thickness from the top and bottom surfaces. The transverse shear stress σ_{13} has very small magnitude on the ceramic and metal phase surfaces as 'n' is increased. However, it is higher on the ceramic surface than that on the metal surface for $n = 0.1$, whereas it is higher on the metal surface for $n = 10.0$. In addition, the shearing stresses on both the ceramic-rich and the metal-rich surfaces act in opposite directions. It is evident that the transverse shear stress may contribute the interlayer failure for $n > 2.0$. A uniform transverse shearing stress σ_{13} variation through the plate thickness can be obtained for $n = 1.0$–2.0. However, the main reason of material failure is the longitudinal normal stresses σ_{11} and σ_{22}. In addition, $n = 0.5$ results in the lowest transverse shearing stress σ_{13} variation. However, the optimum compositional gradient exponent n providing a minimum transverse shearing stress variation can be determined using the optimization techniques.

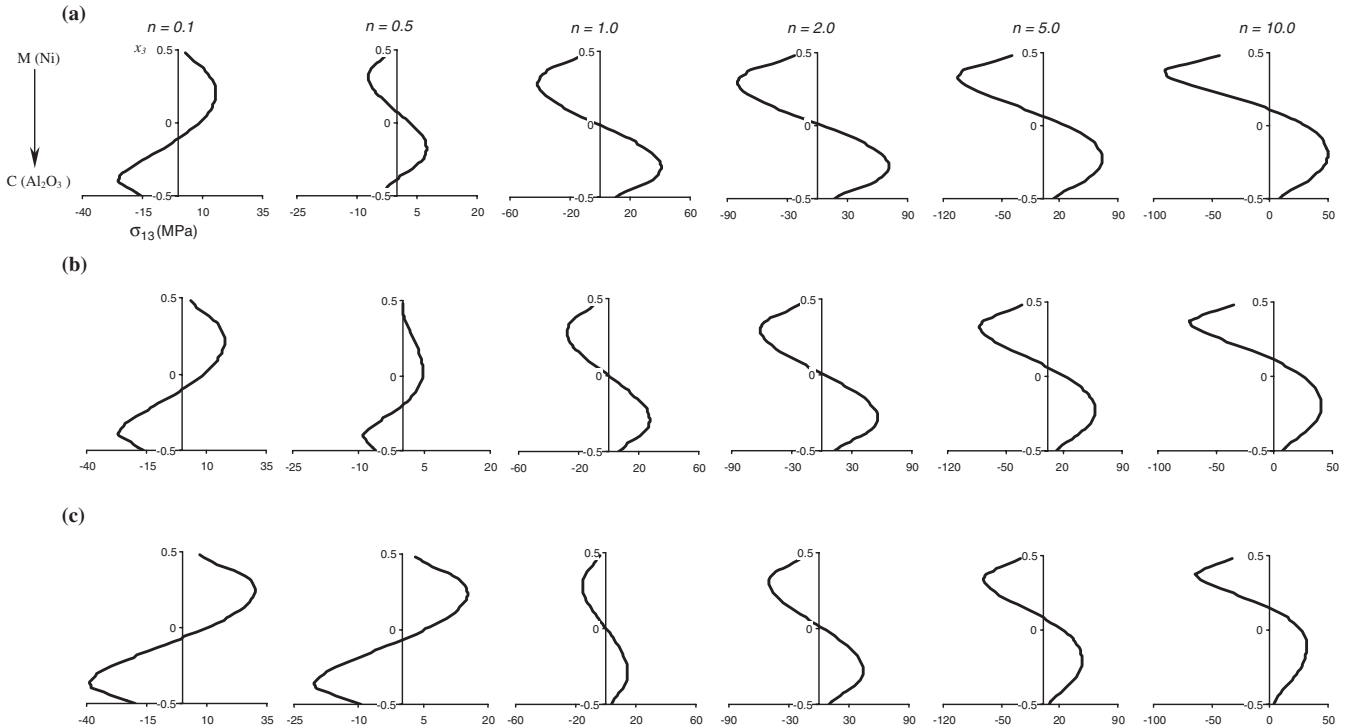

Figure 8. *The effect of the compositional gradient exponent n on the through-thickness variation of the transverse shear stress σ_{13} in Ni–Al_2O_3 functionally graded plates subjected to: (a) uniform; (b) linear; and (c) parabolic temperature fields (stresses in MPa).*

Ni–TiO_2 SYSTEM

The thermal residual stress analysis of a Ni–TiO_2 functionally graded composite plate was also carried out for a uniform temperature field in order to investigate the effect of different constituents on thermal residual stresses. A compositional gradient exponent $n < 1.0$ results in compressive longitudinal stress σ_{11} on both the ceramic and the metal surfaces. Especially, the ceramic surface experiences severe compressive stresses, and a large region through the middle plate thickness is subjected to small tensile stresses as shown in Figure 9(a). As the compositional gradient exponent is increased the longitudinal stress σ_{11} increases considerably and it becomes tensile on the ceramic and the metal surfaces. However, the increase in the normal stress σ_{11} on the metal surface is more obvious. In addition, a large region around the middle plane of the plate is still in compression.

The comparison of the longitudinal stress σ_{11} to those in the Ni–Al_2O_3 functionally graded plate (Figure 7(a)) shows that the profile of the through-thickness variation of the longitudinal stress σ_{11} remained the same. The normal stresses σ_{11} on the ceramic-rich region are similar since the constituents TiO_2 and Al_2O_3 have close mechanical and thermal properties. Even though the metal constituent is Ni in both Ni–TiO_2 and Ni–Al_2O_3 the normal stresses σ_{11} are lower by 90 and 60% in the Ni–Al_2O_3 functionally graded plates with $n = 1.0$ and 10.0, respectively. The coefficient of thermal expansion of TiO_2 ($\alpha_{TiO_2} = 8.9 \times 10^{-6}/^{\circ}C$) is larger than that of Al_2O_3 ($\alpha_{Al_2O_3} = 7.4 \times 10^{-6}/^{\circ}C$) as shown in Table 1, whereas the metal contituent Ni has $\alpha_{Ni} = 15\times\ 10^{-6}/^{\circ}C$. A simple calculation indicates that the thermal strain difference $\Delta\varepsilon^t = (\alpha_{Ni} - \alpha_{Al_2O_3})\Delta T = 7.6 \times 10^{-6}/^{o}C$ in Ni–Al_2O_3 system is higher than the thermal strain difference in Ni–TiO_2 system $\Delta\varepsilon^t = (\alpha_{Ni} - \alpha_{TiO_2})\ \Delta T = 6.1 \times 10^{-6}/^{o}C$. Therefore, a lower longitudinal stress σ_{11} can be expected in Ni–TiO_2 functionally graded plate than those in Ni–Al_2O_3 functionally graded plate as shown in Figures 7(a) and 9(a), respectively. The coefficient of thermal expansion of the ceramic constituent of functionally graded plate plays a very important role on the magnitudes of thermal residual longitudinal stress σ_{11} variation, but does not affect the profile of the through-thickness σ_{11} variation. Therefore, the use of the ceramic and the metal constituents having close thermal expansion coefficients reduces thermal strain difference between the metal and the ceramic constituents, accordingly the thermal residual stresses.

The through-thickness variations of the transverse shear stress σ_{13} in the Ni–TiO_2 functionally graded plate are shown in Figure 10(a). Ni–TiO_2 functionally graded plate exhibits similar transverse shear stress variations (Figure 10(a)) to those in Ni–Al_2O_3 functionally graded plate (Figure 8(a)), for all the compositional gradient components $n = 0.1$–10.0. Thus, the ceramic and the metal constituents do not affect the profile of the transverse

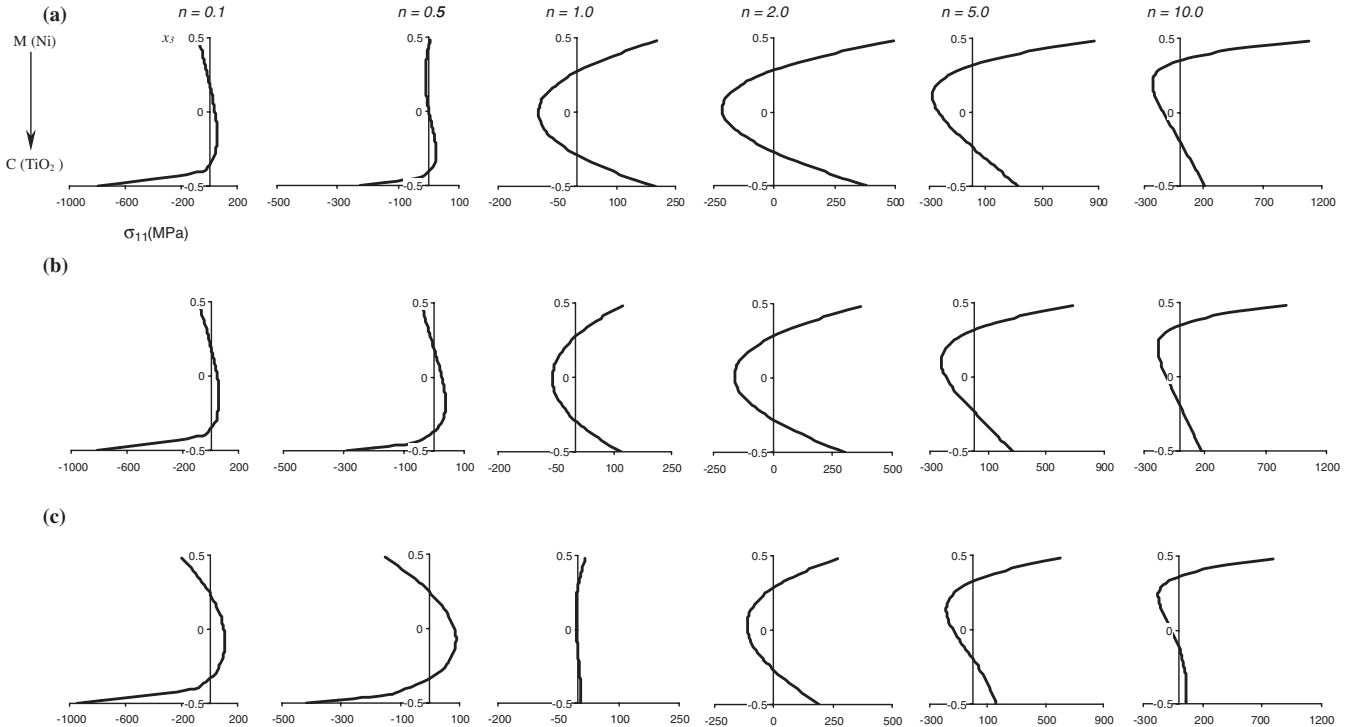

Figure 9. *The effect of the compositional gradient exponent n on the through-thickness variation of the longitudinal stress σ_{11} in Ni–TiO_2 functionally graded plates subjected to: (a) uniform; (b) linear; and (c) parabolic temperature fields (stresses in MPa).*

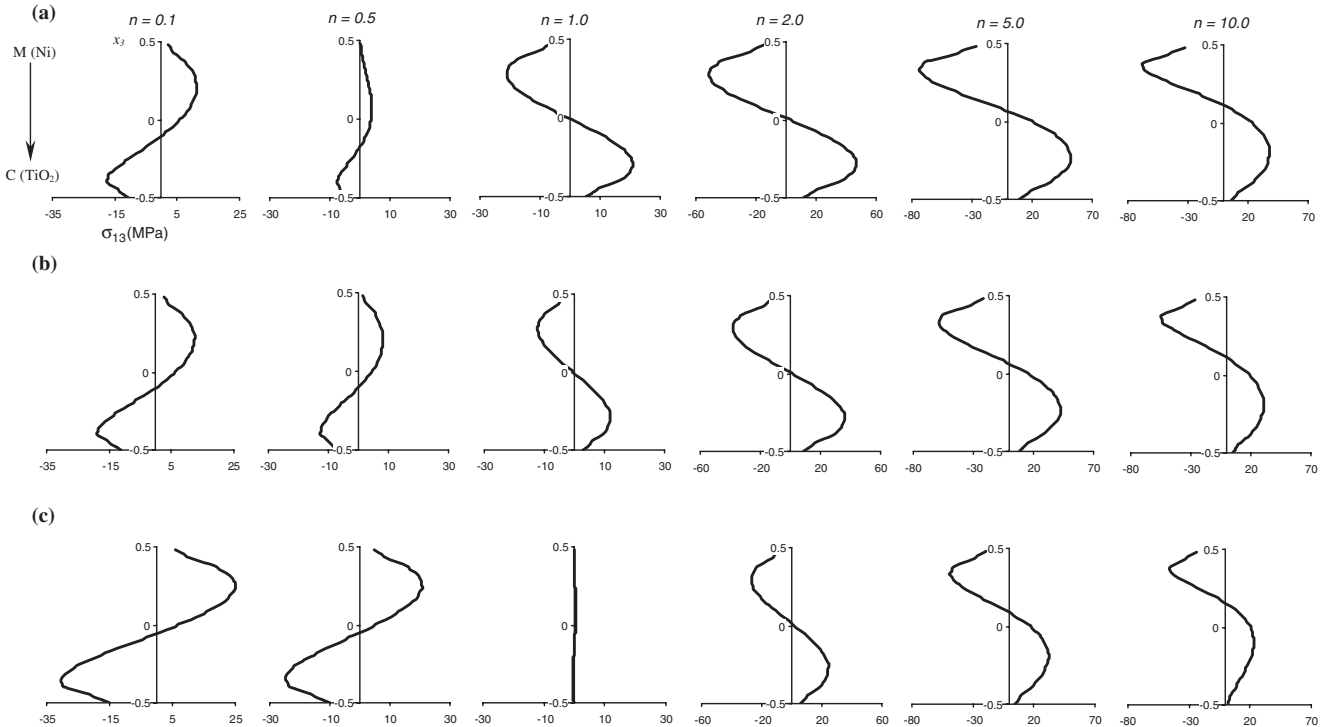

Figure 10. *The effect of the compositional gradient exponent n on the through-thickness variation of the transverse shear stress σ_{13} in Ni–TiO_2 functionally graded plates subjected to: (a) uniform; (b) linear; and (c) parabolic temperature fields (stresses in MPa).*

shear stress σ_{13} variation through the plate thickness. Whereas the magnitude of the shear stress σ_{13} on the ceramic- and metal-rich regions are reduced by 27% for $n = 1.0$ and 14% for $n = 10.0$ (Figures 8(a) and 10(a)).

As a result, the thermal and mechanical properties of the ceramic constituent have considerable effect on the magnitudes of the longitudinal stress σ_{11} and the transverse shearing stress σ_{13} through the plate thickness rather than on the profiles of their through-thickness variations.

Ti–SiC SYSTEM

In addition, the thermal residual stress in a Ti–SiC functionally graded plate with constituents of Young's modulus ratio $E_c/E_m = 4.318$ and difference of the coefficients of thermal expansion $\alpha_m - \alpha_c = 5.8 \times 10^{-6}/^{\circ}\mathrm{C}$, were investigated in order to determine the effect of both the modulus ratio and the ratio of coefficients of thermal expansion of metal and ceramic on the thermal residual stresses. The modulus ratios of Ni–Al_2O_3 and Ni–TiO_2 are 2.71 and 2, respectively. The through-thickness variation of the longitudinal stress σ_{11} in Ti–SiC system is shown in Figure 11(a). It was observed that the modulus and expansion coefficient ratios had a small effect on the through-thickness profile of the normal stress σ_{11} whereas its effect was considerable on its magnitude. Although the modulus of SiC is higher than those of both TiO_2 and Al_2O_3, the normal stress σ_{11} in the ceramic-rich region was lower (Figure 11(a)) than those in Ni–Al_2O_3 (Figure 7(a)) and Ni–TiO_2 (Figure 9(a)) functionally graded plates. In addition, the through-thickness variations of the transverse shear stress σ_{13} are similar to those in Ni–Al_2O_3 (Figure 8(a)) and Ni–TiO_2 (Figure 10(a)) functionally graded plates, and considerable increases in their magnitude are observed as the compositional gradient exponent n is increased (Figure 12(a)).

Finally, we can conclude that the dominant factor on the thermal residual longitudinal stress σ_{11} and transverse shear stress σ_{13} is the difference of the coefficients of thermal expansion of the metal and the ceramic constituents of functionally graded plates subjected to a uniform temperature field rather than the ratio of their Young's modulus. Therefore, the fact that the metal and the ceramic constituents have close thermal properties will be beneficial in reducing the thermal residual normal and shear stresses through the plate thickness.

Linear Temperature Variation

The Ni–Al_2O_3, Ni–TiO_2, and Ti–SiC functionally graded composite plates were analyzed for a through-thickness linear temperature field defined as

$$\Delta T(x_3) = 200\left(\frac{x_3}{h}\right) - 875 \tag{39}$$

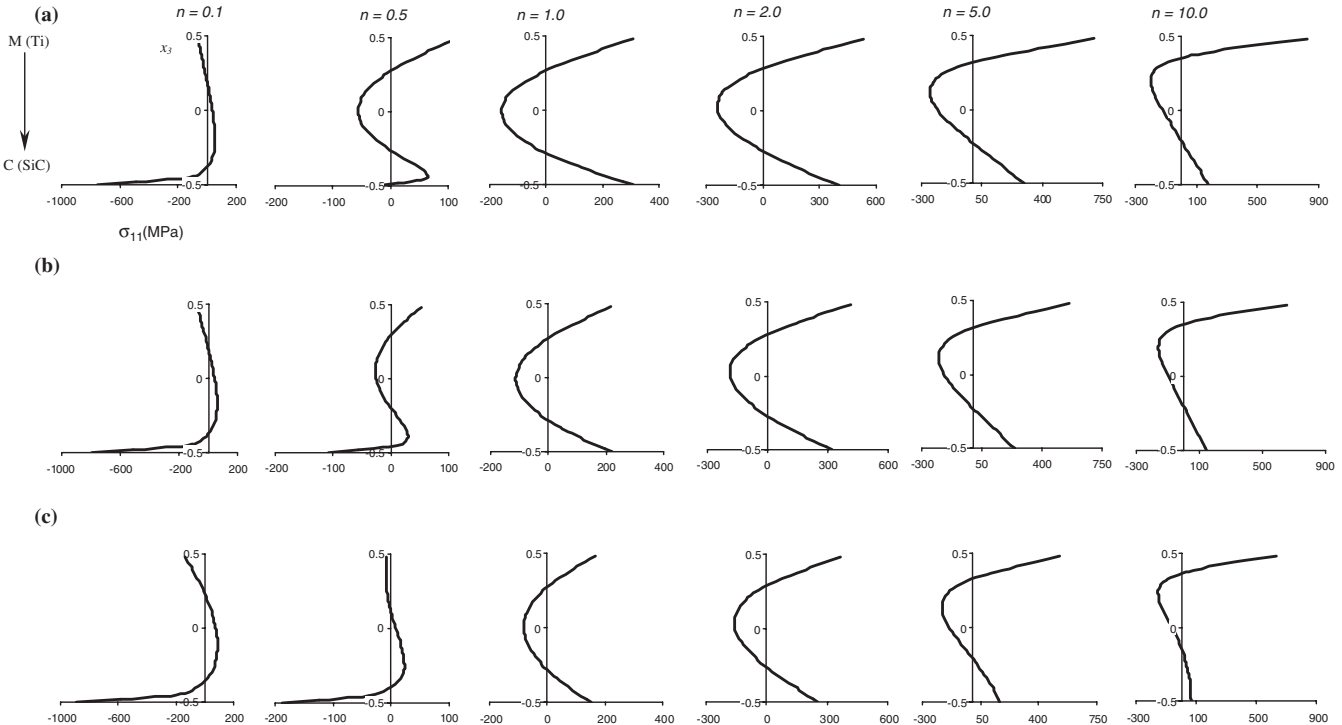

Figure 11. *The effect of the compositional gradient exponent n on the through-thickness variation of the longitudinal stress σ_{11} in Ti–SiC functionally graded plates subjected to: (a) uniform; (b) linear; and (c) parabolic temperature fields (stresses in MPa).*

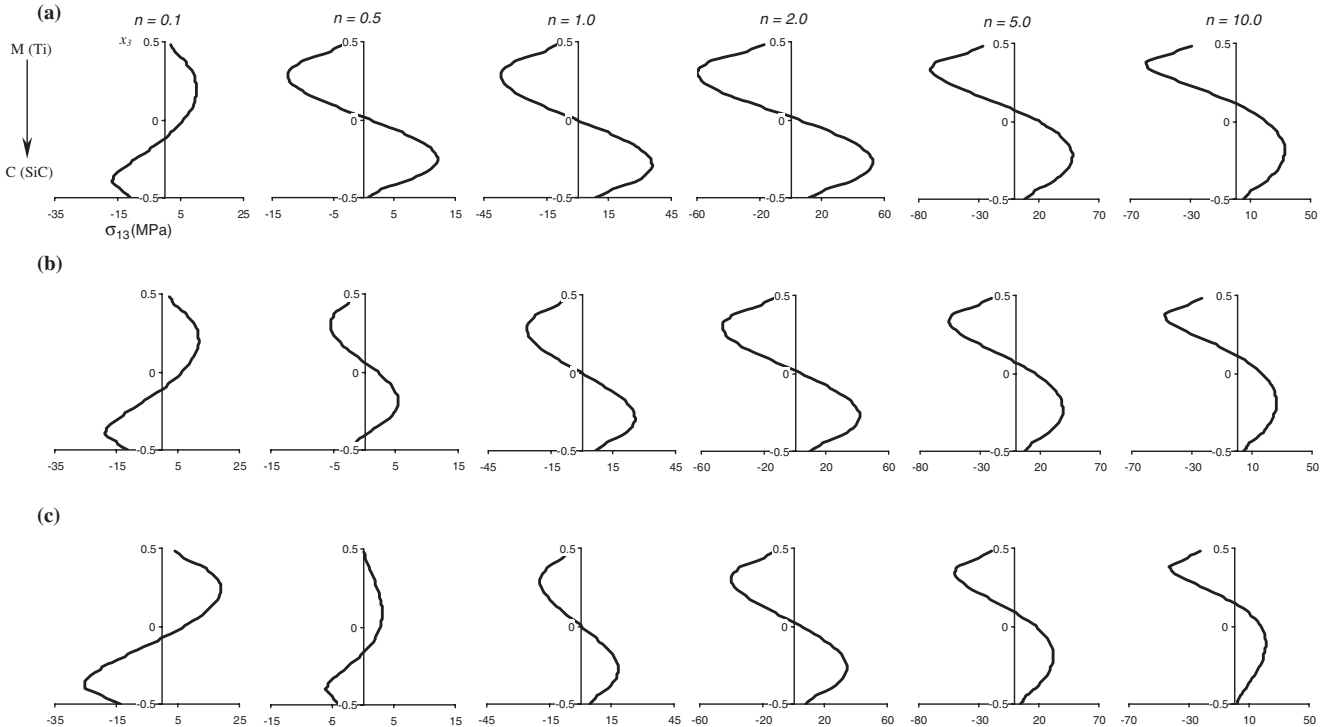

Figure 12. *The effect of the compositional gradient exponent n on the through-thickness variation of the transverse shear stress σ_{13} in Ti–SiC functionally graded plates subjected to: (a) uniform; (b) linear; and (c) parabolic temperature fields (stresses in MPa).*

where x_3 is the distance through the plate thickness h. The thermal stress analyses of three Ni–Al_2O_3, Ni–TiO_2, and Ti–SiC functionally graded plates were carried out for the compositional gradient exponents $n = 0.1$–10.0. The through-thickness variations of the longitudinal residual stress σ_{11} of Ni–Al_2O_3, Ni–TiO_2, and Ti–SiC functionally graded plates are shown in Figures 7(b), 9(b), and 11(b), respectively. The Ni–Al_2O_3 system exhibits similar normal σ_{11} stress variations to those in the case of the uniform temperature field (Figure 7(a)). Thus, the profiles of the normal stress σ_{11} are not affected considerably. However, the normal stress σ_{11} decreases and changes to compressive state from tensile for $n = 1.0$. Similarly, the temperature distribution has small effect on the variation of the transverse shearing stress σ_{13} through the plate thickness as shown in Figures 8(b), 10(b), and 12(b) for Ni–Al_2O_3, Ni–TiO_2, and Ti–SiC functionally graded plates, respectively. The profile of the transverse shearing stress σ_{13} changes slightly and its magnitude decreases in comparison with those in the uniform temperature field (Figures 8(a), 10(a), and 12(a)). The differences in the magnitudes of the normal stress σ_{11} and shear stress σ_{13} are due to the difference of thermal expansion coefficients rather than the temperature field type.

Parabolic Temperature Variation

Finally, the thermal residual stress analyses of the Ni–Al_2O_3, Ni–TiO_2, and Ti–SiC functionally graded plates were investigated for the compositional gradient exponents $n = 0.1$–10.0 and for a parabolic temperature variation defined as

$$\Delta T(x_3) = -775 - \frac{200}{h^2}\left(x_3 - \frac{h}{2}\right)^2 \tag{40}$$

The through-thickness variations of the longitudinal stress σ_{11} for three material systems are shown in Figures 7(c), 9(c), and 11(c), respectively. In cases $n = 0.1$ and 0.5 the normal stress σ_{11} becomes tensile in a large middle region of plate thickness. In general, the normal stress σ_{11} decreases negligibly and the profile of the through-thickness variation of the normal stress σ_{11} does not change considerably. The present uniform, linear, and parabolic temperature distributions result in the normal stress σ_{11} to have a similar through-thickness variation with different magnitudes. The transverse shear stress σ_{13} has also similar through-thickness variations for three functionally graded plates as shown in Figures 8(c), 10(c), and 12(c). In cases $n = 0.1$ and 0.5 the shearing stress σ_{13} becomes higher than those in

the uniform and linear temperature distributions, but it is smaller for $n = 1.0$–10.0. The profiles of the shear stress σ_{13} variation through the functionally graded plates remain almost the same whereas they are different in magnitude.

The thermal stress analysis of the functionally graded plates with different constituents shows that continuous thermal fields through the plate thickness do not affect considerably the through-thickness profiles of both the longitudinal stress σ_{11} and the transverse shear stress σ_{13}. The magnitudes of the normal and shear stresses are strongly dependent on the difference in the coefficients of thermal expansion of the constituents of the functionally graded plates.

CONCLUSIONS

This study investigates the thermal residual stresses in the Ni–Al_2O_3, Ni–TiO_2, and Ti-SiC functionally graded plates subjected to the uniform, linear, and parabolic thermal fields through the plate thickness. A 3D layered isoparametric finite element was implemented to the thermal residual stress problem of a functionally graded plate modeled with 2500 layers through the plate thickness. The following results can be concluded:

(i) The longitudinal stress σ_{11} is dominant among the stress components. It becomes compressive on the ceramic- and the metal-rich regions for compositional gradient exponents $n = 0.1$ and 0.5 whereas it is tensile on both the ceramic-rich and the metal-rich regions and compressive in the middle of the plate thickness for $n > 0.5$.

(ii) The transverse shear stress σ_{13} becomes important along the free edges of the plate and has a symmetric variation through the plate thickness. The metal- and the ceramic-rich regions experience low shear stress σ_{13} which becomes maximal inside the plate. There is also one plane along which shear stress σ_{13} is zero.

(iii) The thermal and mechanical properties of the constituents of the functionally graded plates affect considerably the through-thickness profiles of the normal stress σ_{11} and shear stress σ_{13} variations. In particular, the difference in the coefficients of thermal expansion of the constituents plays an important role in the magnitudes of both the residual normal and shear stresses.

(iv) The modulus of elasticity of the ceramic constituent had a small effect on the normal and shear stresses contrary to its coefficient of thermal expansion.

(v) Finally, the continuous temperature fields through the plate thickness result in similar normal σ_{11} and shear σ_{13} stress variations.

REFERENCES

1. Ahmad, S., Irons, B.M. and Zienkiewicz, O.C. (1970). Analysis of Thick and Thin Shell Structures by Curved Finite Elements, *Int. J. of Numerical Methods in Engineering*, **2**: 419–451.
2. Yunus, S.M. and Khonke, P.C. (1989). An Efficient Through-Thickness Integration Scheme in an Unlimited Layer Doubly Curved Isoparametric Composite Shell Element, *Int. J. of Numerical Methods in Engineering*, **28**: 2777–2793.
3. Koizomi, M. (1997). FGM Activities in Japan, *Composites Part B*, **28B**: 1–4.
4. Takemura, M., Yoshitake, A., Hayakaurad, H., Hyakubu, T. and Tamura, M. (1990). Mechanical and Thermal Properties of FGM Fabricated by Thin Lamination Method, In: *Proceedings of the 1st Int. Symposium on Functionally Graded Materials Forum*, pp. 97–100.
5. Yoshitake, A., Tamura, M., Shito, I. and Niino, M. (1990). Fabrication of the Functionally Graded Materials, In: *ESA Symposium on Space of Advanced Structural Materials*.
6. Shaw, L.L. (1998). Thermal Residual Stresses in Plates and Coatings Composed of Multi-Layered and Functionally Graded Materials, *Composites Part B*, **29**: 199–210.
7. Reddy, J.N. (2000). Analysis of Functionally Graded Plates, *Int. J. of Numerical Methods in Engineering*, **47**: 663–684.
8. Reddy, J.N. and Cheng, Z.Q. (2001). Three-Dimensional Thermomechanical Deformations of Functionally Graded Rectangular Plates, *Eur. J. Mech. A/Solids*, **20**: 841–855.
9. Cho, J.R. and Oden, J.T. (2000). Functionally Graded Material: A Parametric Study on Thermal-Stress Characteristics Using the Clark-Nicolson-Galerkin Scheme, *Computer Methods in Applied Mechanics and Engineering*, **188**: 17–38.
10. Cho, J.R. and Ha, D.Y. (2001). Averaging and Finite Element Discretization Approach in the Numerical Analysis of Functionally Graded Materials, *Materials Science and Engineering A*, **302**: 187–196.
11. Cho, J.R. and Ha, D.Y. (2002). Volume Fraction Optimization for Minimizing Thermal Stress in Ni-Al_2O_3 Functionally Graded Materials, *Materials Science and Engineering A*, **334**: 147–155.
12. Grujicic, M. and Zhao, H. (1998). Optimization of 316 Stainless Steel/Alumina Functionally Graded Material for Reduction of Damage Induced by Thermal Residual Stresses, *Materials Science and Engineering A*, **252**: 117–132.
13. Becker, T.L., Cannon, R.M. and Ritchie, R.O. (2000). An Approximate Method for Residual Stress Calculation in Functionally Graded Materials, *Mechanics of Materials*, **32**: 85–97.
14. Lidong, T. and Wenchao, L. (2002). Residual Stress Analysis of Ti-ZrO_2 Thermal Barrier Graded Materials, *Materials and Design*, **23**: 627–632.
15. Reiter, T., Dvorak, G.J. and Tvergaard, V. (1997). Micromechanical Models for Graded Composite Materials, *J. Phys. Solids*, **45**: 1281–1302.
16. Reiter, T., and Dvorak, G.J. (1998). Micromechanical Models for Graded Composite Materials II, Thermomechanical Loading, *J. Phys. Solids*, **46**(9): 1655–1673.
17. Grujicic, M. and Zhang, Y. (1998). Determination of Effective Elastic Properties of Functionally Graded Materials Using Voronoi Cell Finite Element Method, *Materials Science and Engineering A*, **251**: 64–74.
18. Tomota, Y., Kuroki, K., Mori, T. and Tamura, T. (1976). Tensile Deformation of Two-Ductile-Phase Alloys: Flow Curves of α-γ Fe-Cr-Ni Alloys, *Materials Science and Engineering*, **24**: 85–94.
19. Wakashima, K. and Tsukamoto, H. (1991). Mean-Field Micromechanics Model and its Application to the Analysis of Thermomechanical Behaviour of Composite Materials, *Materials Science and Engineering A*, **146**: 291–316.

20. Schapery, R.A. (1968). Thermal Expansion Coefficients of Composite Materials, *J. Comput. Materials*, **2**: 380–404.
21. Levin, V.M. (1967). Thermal Expansion Coefficients of Heterogeous Materials, *Mekh. Tverd. Tela*, **2**: 88–94.
22. Cook, R.D., Malkus, D.V. and Plesha, M.E. (1989). *Concept and Applications of Finite Element Analysis*, John Wiley & Sons, Canada.
23. Panda, S. and Natarajan, R. (1981). Analysis of Laminated Composite Shell Structures by Finite Element Method, *Computers and Structures*, **14**: 225–230.
24. Kumar, W.P.P. and Palaninathan, R. (1997). Finite Element Analysis of Laminated Shell with Exact Through-Thickness Integration, *Computers and Structures*, **63**: 173–184.